JGR Planets

RESEARCH ARTICLE

10.1029/2026JE009649

Evolution of a Point Plume in a Rotating Unstratified Fluid Overlain by a Stratified Layer: Scaling and Implications for Icy Satellites

Shuang Wang[1], Wanying Kang[1], Yixiao Zhang[1], and John Marshall[1]

[1]Earth, Atmospheric and Planetary Science Department, Massachusetts Institute of Technology, Cambridge, MA, USA

Key Points:

- Plumes penetrate farther into the stratified layer when rotation is weaker, source is stronger, or the lower unstratified layer is thinner
- A scaling law for the plume penetration height is derived and tested against numerical simulations
- On Europa, it is possible for plumes to reach the ice shell, while on Enceladus and Titan, they likely disperse within the ocean's interior

Supporting Information:

Supporting Information may be found in the online version of this article.

Correspondence to:

S. Wang and W. Kang,
shuangw@mit.edu;
wanying@mit.edu

Citation:

Wang, S., Kang, W., Zhang, Y., & Marshall, J. (2026). Evolution of a point plume in a rotating unstratified fluid overlain by a stratified layer: Scaling and implications for icy satellites. *Journal of Geophysical Research: Planets*, *131*, e2026JE009649. https://doi.org/10.1029/2026JE009649

Received 2 JAN 2026
Accepted 24 JUN 2026

Author Contributions:

Funding acquisition: John Marshall
Investigation: Shuang Wang
Methodology: Shuang Wang, Wanying Kang
Supervision: Wanying Kang, John Marshall
Visualization: Shuang Wang
Writing – original draft: Shuang Wang
Writing – review & editing: Shuang Wang, Wanying Kang, Yixiao Zhang, John Marshall

Abstract Plumes that rise through an unstratified layer and penetrate into an adjacent stably stratified layer are ubiquitous in geophysical and planetary environments, including the subsurface oceans of icy satellites such as Europa, Enceladus, and Titan. In this study, we investigate the evolution of such plumes from isolated buoyant sources, both in non-rotating and rotating systems, with particular emphasis on their penetration height. Non-rotating plumes evolve into a classical "mushroom" structure, whereas rotating plumes evolve into baroclinic cones or can not reach the stratified layer, depending on the interface height h_i. A scaling law for the penetration height z_p is derived in terms of h_i and two characteristic length scales, $L_N \equiv \left(F_0/N^3\right)^{1/4}$ and $L_{\mathrm{rot}} \equiv \left(F_0/f^3\right)^{1/4}$, where F_0 is the buoyancy flux of the source, N is the buoyancy frequency, and $f = 2\Omega$ is the Coriolis parameter (Ω is the rotation rate). In the non-rotating regime, the scaling recovers the classical relation $z_p \propto L_N$ when the unstratified layer is thin and predicts $z_p/L_N \propto (h_i/L_N)^{-1/3}$ when the layer is thick. In the rapid-rotating regime, z_p remains constant for small h_i, followed by a decrease toward zero as h_i increases, due to the lateral mixing by baroclinic eddies. Under weak stratification, plumes typically arrest at about $50L_{\mathrm{rot}}$, independent of h_i. Applying these scalings to icy-ocean worlds suggests that on Europa, plumes could reach the ice shell, whereas on Enceladus and Titan, they are likely arrested in the mid-ocean.

Plain Language Summary In subsurface oceans on icy satellites, heat and chemicals released from the seafloor can rise through the ocean by buoyant plumes. Whether these plumes reach the ice shell above depends on how the density difference between plume water and the ambient ocean changes with depth and how fast the moon is rotating. Using computer simulations, we studied how plumes behave when they rise from an unstratified lower layer into a stably stratified upper layer. We found that rotation and thickness of the lower layer strongly control how far a plume can penetrate. Without rotation, plumes penetrate higher when the lower layer is thin. With rotation, plumes break down and can be stopped by eddies before reaching the surface. Our scaling results suggest that on Europa, plumes likely reach the ice shell, while on Enceladus and Titan, plumes likely stop within the interior of the ocean.

1. Introduction

Icy satellites harboring subsurface oceans, such as Europa (Anderson et al., 1998; Kivelson et al., 2000; Soderlund et al., 2020; S. D. Vance et al., 2018; Zimmer et al., 2000) and Enceladus (Beuthe et al., 2016; Hansen et al., 2006; Hoolst et al., 2016; Iess et al., 2014; Porco et al., 2006; Soderlund et al., 2020; Thomas et al., 2016; S. D. Vance et al., 2018), are prime targets in the search for extraterrestrial life. These oceans are believed to be sustained by heat generated through tidal dissipation in the ice shell or the silicate core (Choblet et al., 2017; Spohn & Schubert, 2003). The heat produced within the rocky interior can be released into the surrounding ocean through hydrothermal systems on the seafloor, which tend to be located near discrete venting sites (S. Vance et al., 2007; Choblet et al., 2017). When the thermal expansivity is positive, as is usually the case except in fresh low-pressure oceans (Kang, Marshall, et al., 2022; S. Vance et al., 2009; Zeng & Jansen, 2021), the localized heat source induces convective plumes that rise through the ocean, transporting heat and tracers to the ice shell (Bire et al., 2023; Goodman & Lenferink, 2012; Goodman et al., 2004; Y. Zhang et al., 2025).

Hydrothermal plumes have also been invoked to explain the surface features of Europa and Enceladus. On Europa, numerous "chaos" terrains, regions of sharp-edged ice blocks embedded in a rough low-lying matrix, are observed (Greeley et al., 2000; Lucchitta & Soderblom, 1982). These features have been interpreted as a result of basal-to-surface melting, with required heat supplied by hydrothermal plumes (Collins et al., 2000; Greenberg

et al., 1999; Thomson & Delaney, 2001). On Enceladus, geyser-like jets have been observed to emanate from the fissure on the south polar ice sheet. Its composition includes water vapor, as well as carbon dioxide (Waite et al., 2006), sodium salt (Postberg et al., 2009), silica particles (Hsu et al., 2015), hydrogen (Waite et al., 2017), and organic compounds (Postberg et al., 2018), consistent with an origin from hydrothermal vents (Hsu et al., 2015).

Most previous studies have assumed that hydrothermal plumes can ascend to the base of the ice shell without significant inhibition, even in oceans that are ten to hundreds of kilometers deep (Collins et al., 2000; Goodman & Lenferink, 2012; Goodman et al., 2004; Thomson & Delaney, 2001). However, recent numerical simulations for unstratified or weakly stratified oceans on Enceladus (Bire et al., 2023; Kang, Marshall, et al., 2022; Y. Zhang et al., 2025) showed that plumes may undergo strong dilution and stall in the mid-ocean, due to rotation-induced baroclinic instabilities that disrupt the plume and divert buoyancy flux laterally (Wang et al., 2025). Similar disruptions may also occur on Europa if the integrated heat flux of a hydrothermal vent is below 0.2 GW (Wang et al., 2025).

Moreover, although icy oceans are broadly convective due to basal heating, a stably stratified layer may form in the upper ocean (Figure 1a). This layer arises because variations in ice thickness modulate the temperature at the ice–ocean interface via the pressure dependence of the freezing point (the Clausius–Clapeyron relation; Kang, 2022; Kang, Bire, & Marshall, 2022; Kang, Mittal, et al., 2022; Lobo et al., 2021; Y. Zhang et al., 2024; Zhu et al., 2017). This stratification can act as a barrier, preventing plumes from reaching the ice shell. These considerations motivate us to study plumes that first grow in an unstratified layer and then penetrate into an overlying stratified layer, with the aim of determining the conditions under which they can deliver heat and materials to the ice shell without significant dilution.

In this paper, we investigate the evolution of a point plume in a partially stratified fluid, consisting of a uniformly stratified layer overlying an unstratified layer (Figure 1a), both with and without rotation. Combining numerical simulations with theoretical analysis, we develop scaling laws for the penetration height of the plume. Section 2 reviews pioneering studies of penetrative plumes in the context of Earth's ocean. The numerical method is introduced in Section 3. Simulation results for non-rotating and rotating plumes are presented in Sections 4 and 5, respectively, followed by the derivation of scaling laws for their terminal heights. Implications for icy satellites are discussed in Section 6. Section 7 offers a brief summary and a discussion. Additional information that is not essential for grasping the content of this paper is available in Supporting Information S1.

2. Previous Work on Penetrative Plumes

Early studies on the penetration of point plumes have been focusing on the non-rotating or weakly rotating scenarios. Considering the simplest configuration, where the entire fluid is uniformly stratified, the penetration height is found to scale with $L_N \equiv \left(F_0/N^3\right)^{1/4}$, where F_0 is the source buoyancy flux, and N is the background buoyancy frequency. Morton et al. (1956) first derived this scaling using a vertically integrated plume model (hereafter MTT), and numerically determined that the proportionality coefficient is around 4. These results were validated against laboratory experiments (Briggs, 1965; Crawford & Leonard, 1962; Turner, 1986; W. Zhang et al., 2017) and numerical simulations (Devenish et al., 2010), and analytically confirmed by asymptotic expansion (Briggs, 1982; Devenish et al., 2010; Scase et al., 2006). When weak rotation is present ($f \ll N$, f is the Coriolis parameter), the plume evolution remains qualitatively similar to the non-rotating scenario during the early evolution, as the plume first feels the stratification rather than rotation. Beyond a time scale $t = f^{-1}$, rotation begins to control the lateral growth of the plume "cap," producing cyclones and anticyclones and triggering baroclinic instability (Speer & Marshall, 1995). Despite the subsequent baroclinic instability, the plume penetration height remains close to $\sim 4L_N$, as in the non-rotating regime.

As f increases, the penetration height is found to decrease relative to the non-rotating scenario (Deremble, 2016; Fabregat Tomàs et al., 2016; Helfrich & Battisti, 1991), since the plume precession induced by the Coriolis effect enhances the dilution of the plume momentum and buoyancy (Fabregat Tomàs et al., 2016; Frank et al., 2017). However, if f further increases to approach or even exceed N, the penetration height increases again, eventually exceeding the value in the non-rotating regime (Deremble, 2016; Fabregat Tomàs et al., 2016; Helfrich & Battisti, 1991), since the strong rotation shuts off the entrainment and concentrates momentum and buoyancy. Besides noting the non-monotonous dependence of penetration height on rotation and the potential competing

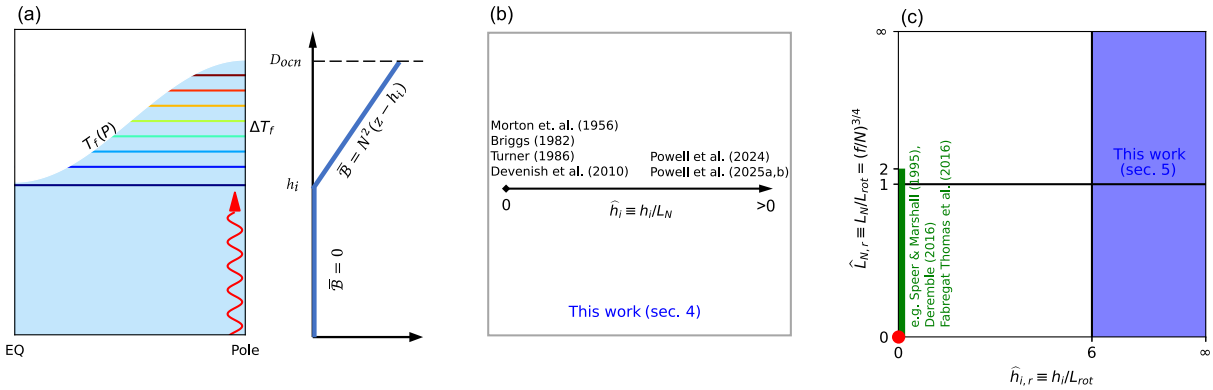

Figure 1. (a) Schematic of a penetrative plume (red spiral arrow) in a partially stratified ocean (blue region). The stratification (colored contours) arises from pressure-dependent variations in the ice–ocean interface temperature ΔT_f imposed by the overlying ice shell (white region). This corresponds to a background buoyancy $\overline{\mathcal{B}} = 0$ below the interface at $z = h_i$ and $\overline{\mathcal{B}} = N^2(z - h_i)$ above. (b) Parameter space for non-rotating penetrative plumes spanned by $\hat{h}_i$. (c) Parameter space for rotating penetrative plumes spanned by $\hat{L}_{N,r}$ and $\hat{h}_{i,r}$. Parameter regimes explored in previous studies and in the present work are marked in these panels.

physical mechanisms, no scaling theory has been proposed for the penetration height when rotation plays an important role.

Beyond uniform stratification, several studies considered penetrative plumes in partially stratified fluids, motivated by atmospheric convection from troposphere to stratosphere and deep convection from the mixed layer to thermocline in the open ocean (Ansong & Sutherland, 2010; Powell, Haynes, et al., 2025; Powell, Sutherland, et al., 2025; Powell et al., 2024). The uniformly stratified scenario can be regarded as an end-member case, where the depth of the lower unstratified layer h_i approaches zero. Although the focus of these works is primarily the excitation of internal gravity waves in the stratified layer, Ansong and Sutherland (2010) found that numerical integration of the MTT model can provide reasonable predictions for the penetration height. However, in all these works, the influence of rotation is neglected.

3. Problem Setup and Numerical Modeling

We perform high-resolution simulations of point plumes using the *Oceananigans.jl*, a GPU-accelerated large-eddy simulation (LES) framework (Ramadhan et al., 2020). The model solves the non-hydrostatic Boussinesq equations,

$$\nabla \cdot \boldsymbol{u} = 0, \tag{1}$$

$$\frac{\partial \boldsymbol{u}}{\partial t} = -\boldsymbol{u} \cdot \nabla \boldsymbol{u} - \nabla \mathcal{P} - f\boldsymbol{k} \times \boldsymbol{u} + \mathcal{B}\boldsymbol{k} + \nu \nabla^2 \boldsymbol{u}, \tag{2}$$

$$\frac{\partial \mathcal{B}}{\partial t} = -\boldsymbol{u} \cdot \nabla \mathcal{B} + \kappa \nabla^2 \mathcal{B}, \tag{3}$$

where $\boldsymbol{u}$ is the velocity vector in Cartesian coordinates, $\boldsymbol{k}$ is the unit vector in the vertical direction (z), $\mathcal{B}$ is the buoyancy, $\mathcal{P}$ is the pressure, and ν and κ are the viscosity and diffusivity, respectively. Note that $\mathcal{B}$ and $\mathcal{P}$ can be divided into

$$\mathcal{B} = \overline{\mathcal{B}} + b, \quad \mathcal{P} = \overline{\mathcal{P}} + p, \quad \overline{\mathcal{B}} - \frac{\partial \overline{\mathcal{P}}}{\partial z} = 0, \tag{4}$$

where $\overline{\mathcal{B}}$ is the background buoyancy, b is the buoyancy perturbation, $\overline{\mathcal{P}}$ is the hydrostatic pressure, and p is the non-hydrostatic pressure. In the subsequent analysis, we focus on b and p, since they capture the plume-induced deviations from the background state and directly govern the plume dynamics.

By default, the model employs a high-order weighted essentially non-oscillatory advection scheme, which stabilizes the solution by providing an effective adaptive hyper-viscosity based on local smoothness (Shu, 2009). No explicit turbulence closure is required, and this setup is commonly referred to as an implicit LES (iLES; Silvestri et al., 2024).

The domain is rectangular, extending from $-L/2$ to $L/2$ in both the $x-$ and $y-$directions with doubly periodic boundary conditions and ranging from $z = 0$ to $z = H$ in the $z-$direction. At the top, we use a stress-free condition for velocity and a no-flux condition for buoyancy, that is,

$$w = 0, \quad \frac{\partial^2 w}{\partial z^2} = 0, \quad \frac{\partial \mathcal{B}}{\partial z} = 0 \quad \text{at } z = H, \tag{5}$$

where w is the vertical velocity. This setup corresponds to a scenario in which the time scale of heat and momentum exchange between the plume and the surface is much longer than the convective timescale. At the bottom, we also use the stress-free condition, but set a buoyancy flux F_A (units: $\mathrm{m^2\ s^{-3}}$) concentrated within a radius circle r_s,

$$w = 0, \quad \frac{\partial^2 w}{\partial z^2} = 0, \quad F_A = \frac{F_0}{\pi r_s^2} \exp\left(-\frac{x^2 + y^2}{r_s^2}\right). \tag{6}$$

Here, F_0 is the source buoyancy flux in units of $\mathrm{m^4\ s^{-3}}$. The whole domain rotates along the $z-$axis, resulting in a Coriolis parameter f. The initial velocity is zero. The background buoyancy is initialized as zero below an interface at $z = h_i$ and increases linearly above it following $N^2(z - h_i)$. We also add small-amplitude noise in the initial buoyancy field to trigger shear instabilities naturally near the source, accelerating the transition from laminar to turbulent flow.

In this configuration, in total there are five external parameters F_0, f, N, h_i, and r_s. The radius r_s has negligible effect on the bulk dynamics of the plume, when it is sufficiently small for it to be treated as a geometric point (Wang et al., 2025). The remaining four parameters can be reformulated into two characteristic length scales

$$L_N \equiv \left(\frac{F_0}{N^3}\right)^{1/4}, \quad L_{\mathrm{rot}} \equiv \left(\frac{F_0}{f^3}\right)^{1/4}, \tag{7}$$

and the ratio between these two length scales and h_i gives two nondimensional numbers that govern the dynamics of the system,

$$\left(\hat{L}_{N,r},\ \hat{h}_{i,r}\right) \equiv \left(\frac{L_N}{L_{\mathrm{rot}}},\ \frac{h_i}{L_{\mathrm{rot}}}\right), \tag{8}$$

where the notation $\widehat{(\cdot)}$ denotes a dimensionless quantity, and the subscript "r" indicates the presence of background rotation. The former nondimensional number characterizes the relative importance between N and f, and the latter characterizes whether the rotation is important on the plume that impinges on the interface between stratified and unstratified layers (Fernando et al., 1998; Goodman et al., 2004). As illustrated in Figure 1c, the parameter space spanned by them can be divided into four regimes by $\hat{L}_{N,r} = 1$ and $\hat{h}_{i,r} = 6$. Note that in the non-rotating limit where $f \to 0$ and $L_{\mathrm{rot}} \to \infty$, both $\hat{L}_{N,r}$ and $\hat{h}_{i,r}$ vanish. In this limit, we instead define the dimensionless parameter

$$\hat{h}_i \equiv \frac{h_i}{L_N}. \tag{9}$$

To avoid ambiguity, we emphasize that in this study $\hat{h}_i = 0$ always results from $h_i = 0$ (i.e., the absence of an unstratified layer) rather than from $N = 0$ (unstratified environment), because in the latter case, the definition of plume penetration height is invalid.

Table 1
Parameters Used for Simulations in Non-Rotating (Upper) and Rapid-Rotating (Lower) Regimes

Non-rotating regime									
$\hat{h}_i$	0.02	0.06	0.11	0.21	0.53	1.06	2.11	3.17	4.23
	5.29	7.93	8.89	15.8	29.7	50.0	88.9	167	281
Rapid-rotating regime									
$\hat{L}_{N,r}$	31.6, 3.3, 1.7, 1, 0.6, 0.3								
$\hat{h}_{i,r}$	10, 12, 14, 16, 18, 20, 25, 30, 35, 40, 50, 60, 70								

Note. In the non-rotating regime, the domain is cubic with size $L = H = 1000$ m, horizontal and vertical grid spacings $\Delta_h = \Delta_z = 2$ m, and source radius $r_s = 2$ m. In the rapid-rotating regime, the dimensionless values of them are fixed at $\hat{L}_r = 20$, $\hat{H}_r = 75$, $\hat{\Delta}_{h,r} = \hat{\Delta}_{z,r} = 0.05$, and $\hat{r}_{s,r} = 0.1$.

To place our study in context, Figures 1b and 1c show the parameter space with regimes investigated in previous studies and the present one. Many early studies (e.g., Briggs, 1982; Devenish et al., 2010; Morton et al., 1956; Turner, 1986) examined the penetration of a point plume into a uniformly stratified fluid immediately after emission from the source ($h_i = 0$) in a non-rotating environment ($L_{\text{rot}} \to \infty$). These conditions correspond to the origin of the axis in Figure 1b. Ansong and Sutherland (2010), Powell et al. (2024), Powell, Haynes, et al. (2025), and Powell, Sutherland, et al. (2025) extended this framework by introducing an unstratified layer beneath the stratified layer ($h_i > 0$). The corresponding part of the parameter space is represented by the rest of the axis in Figure 1b. The role of rotation was subsequently explored in the uniformly stratified fluid (e.g., Deremble, 2016; Fabregat Tomàs et al., 2016; Speer & Marshall, 1995), where $\hat{L}_{N,r}$ is considered up to 2, indicated by the green line in Figure 1c. The present study focuses on a two-layer configuration with an unstratified lower layer overlain by a stratified upper layer ($h_i \geq 0$). We investigate two scenarios: (a) a non-rotating regime ($L_{\text{rot}} \to \infty$) and (b) a rapidly rotating regime, defined by $\hat{h}_{i,r} > 6$, in which the plume becomes rotation-dominated before reaching the interface at height h_i. These two regimes are marked by the axis in Figure 1b and the blue region in Figure 1c.

We conduct numerical simulations for the non-rotating and rotating regimes, separately, with parameter choice summarized in Table 1. In the non-rotating regime, the simulation parameters are nondimensionalized by L_N (referred to as $\widehat{(\cdot)}$) and N. However, the domain size is instead prescribed as a sufficiently large dimensional value, while the grid spacing and source radius are prescribed as sufficiently small dimensional values. This is because the plume is self-similar in the unstratified layer and lacks a characteristic scale L_N. Specifically, the domain has horizontal and vertical extents $L = H = 1000$ m, the horizontal and vertical grid spacings are $\Delta_h = \Delta_z = 2$ m, and the source radius is $r_s = 2$ m. Instead, in the rapid-rotating regime, the parameters, as well as the domain size and grid size, are nondimensionalized by the rotational length scale L_{rot} (referred to as $\widehat{(\cdot)}_r$) and the Coriolis parameter f, as the plume dynamics is governed by rotation (Bire et al., 2023; Fernando et al., 1998; Goodman et al., 2004). The dimensionless domain horizontal and vertical extents are $\hat{L}_r = 20$ and $\hat{H}_r = 75$, respectively; the dimensionless grid size is set to 0.05 in both horizontal and vertical directions; and the dimensionless source radius is $\hat{r}_{s,r} = 0.1$. These configurations are adopted from Wang et al. (2025), which demonstrated that source radius has minimal influence on terminal height in unstratified conditions and that the resolution adequately captures rotating point plume evolution and ensures numerical convergence for plume terminal height.

In order to diagnose the plume morphology, we continuously release passive tracers from the source. The tracer concentration c obeys the same governing equation as b, with the same diffusivity, and boundary conditions. The plume boundary is defined by an envelope $c/c_s = 10^{-4}$, where the subscript "s" denotes the value at the source. For a non-rotating plume, this boundary is clearly identified in the $x - z$ cross section at $y = 0$. However, for a rotating plume, the boundary is not adequately shown in the $y = 0$ section because the primary plume separates to several secondary plumes that drift away. To address this, we average c along the y−axis ($\overline{c}^y$) and use the envelope $\overline{c}^y/\overline{c}^y_s = 10^{-3}$ to distinguish between the plume and the ambient fluid in this effective side view. The threshold values used for the envelopes are sufficiently small to capture the majority of the extent of the plume, and our results are insensitive to the use of smaller threshold values (Wang et al., 2025).

4. Point Plumes in the Non-Rotating Regime

4.1. Plume Evolution and Comparison With the MTT Model

The evolution of a non-rotating point plume is illustrated in Figure 2, based on a simulation with $\hat{h}_i = 5$. Other simulations exhibit qualitatively similar results.

In the early stage, the plume rises in the lower unstratified layer because the source fluid is more buoyant than the environment. Shear develops between the rising plume and the quiescent surroundings and triggers Kelvin-Helmholtz instabilities, which generate turbulence that entrains ambient fluid into the plume. This causes the

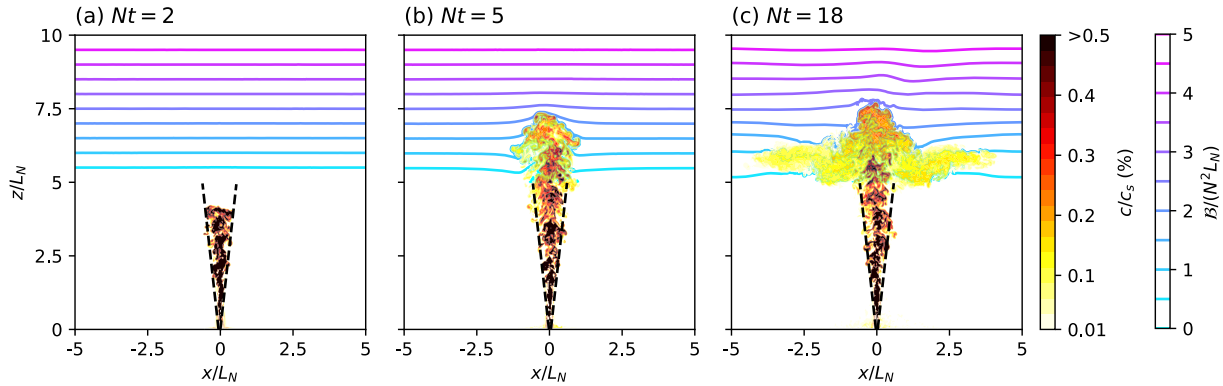

Figure 2. Instantaneous $x - z$ cross-sections along $y = 0$ showing the dimensionless tracer concentration c/c_s (color shading) and buoyancy $\mathcal{B}$ (contours) from the simulation with $F_0 = 10^{-5}$ m^4 s^{-3}, $N = 5 \times 10^{-5}$ s^{-1}, and $h_i = 500$ m (corresponding to $\hat{h}_i = 5.29$). The predicted plume boundary in the lower unstratified layer (Equation 16) is represented by black dashed lines.

plume to expand laterally and develop a characteristic conical shape (Figure 2a) until it reaches the interface between the unstratified and stratified layers. Soon after, the plume front becomes denser than the ambient fluid but, despite this, inertia enables the plume to overshoot a finite distance before its vertical velocity decreases to zero (Figure 2b). Thereafter, the plume subsides from the terminal height back to the neutral height where buoyancy vanishes and intrudes laterally, forming the classic "mushroom" structure (Figure 2c). These behaviors are consistent with previous laboratory experiments (e.g., Ansong & Sutherland, 2010) and numerical simulations (e.g., Powell, Sutherland, et al., 2025; Powell et al., 2024).

It has been shown that the evolution of point plumes can be well-captured by the MTT model, a set of ordinary differential equations (ODEs) that describes the conservation of mass, momentum and buoyancy (Morton et al., 1956). To derive the ODEs of the MTT model, one needs to assume that (a) the plume is axisymmetric and steady, (b) the vertical gradient of non-hydrostatic pressure p is small compared to buoyancy perturbation b, and (c) the mean radial velocity of the entrained inflow u_e is proportional to the vertical velocity w in the center of the plume (entrainment hypothesis), with an entrainment coefficient α. With these assumptions, the steady-state Boussinesq equations (Equations 1–3) reduce to

$$\frac{\mathrm{d}Q}{\mathrm{d}z} = 2\alpha\xi(\pi M)^{\frac{1}{2}}, \tag{10}$$

$$\frac{\mathrm{d}M}{\mathrm{d}z} = \frac{FQ}{M}, \tag{11}$$

$$\frac{\mathrm{d}F}{\mathrm{d}z} = -N^2 Q. \tag{12}$$

Here, Q, M, and F denote vertical fluxes of volume, momentum, and buoyancy, respectively, that is,

$$Q = \iint w(r,z) r \mathrm{d}r\mathrm{d}\theta, \quad M = \iint w(r,z)^2 r \mathrm{d}r\mathrm{d}\theta, \quad F = \iint w(r,z) b(r,z) r \mathrm{d}r\mathrm{d}\theta, \tag{13}$$

where r is the radius, θ is the azimuth, and ξ is a geometric factor depending on the radial distributions of w and b.

For a plume in an unstratified environment ($N = 0$), the w and b profiles are assumed to decay radially from the center of the plume following a Gaussian profile (Figure 3b; also see Morton et al., 1956),

$$w(r,z) = W(z)\exp\left[-\frac{r^2}{R(z)^2}\right], \quad b(r,z) = B(z)\exp\left[-\frac{r^2}{R(z)^2}\right]. \tag{14}$$

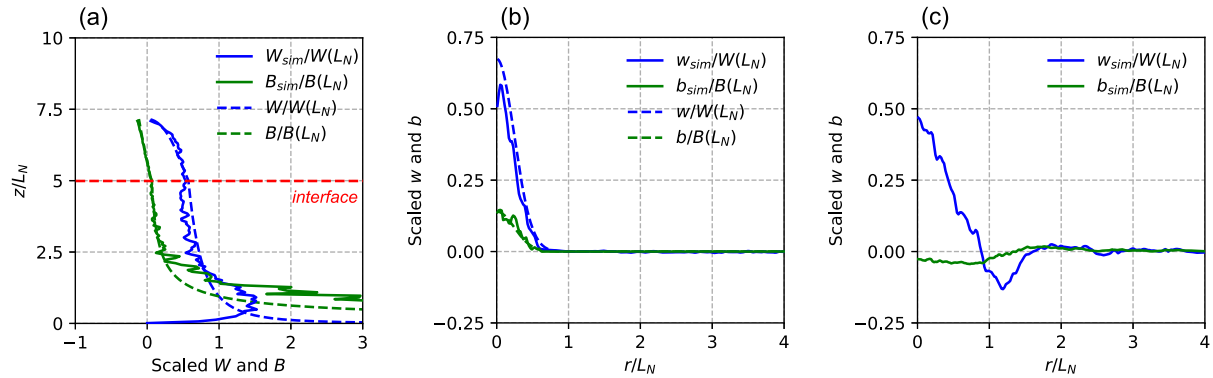

Figure 3. (a) Vertical profiles of w and b along the plume centerline. (b and c) Radial distributions of w and b as functions of $r = \sqrt{x^2 + y^2}$ at $z/L_N = 3$ and $z/L_N = 6$, respectively, corresponding to Figure 2c. Solid and dashed curves show the simulation results and theoretical predictions obtained by integrating Equations 10–12, respectively. Both w and b are scaled by their corresponding theoretical values at $z = L_N$ from Equation 16. In panel (a), the red dashed line represents the interface height.

Under such assumption, Equation 13 gives the geometric factor $\xi = \sqrt{2}$, and laboratory measurements yield the entrainment coefficient $\alpha_u = 0.093$ (Morton et al., 1956; Turner, 1986), where the subscript "u" denotes the unstratified case. Under this circumstance, the MTT model (Equations 10–12) can be analytically solved as

$$Q = \frac{6\pi\alpha_u}{5}\left[\frac{9\alpha_u}{5}\left(\frac{2F_0}{\pi}\right)\right]^{\frac{1}{3}} z^{\frac{5}{3}}, \quad M = \frac{\pi}{2}\left[\frac{9\alpha_u}{5}\left(\frac{2F_0}{\pi}\right)\right]^{\frac{2}{3}} z^{\frac{4}{3}}, \quad F = F_0, \tag{15}$$

or equivalently as

$$R = \frac{6}{5}\alpha_u z, \quad W = \frac{5}{6\alpha_u}\left[\frac{9\alpha_u}{5}\left(\frac{2F_0}{\pi}\right)\right]^{\frac{1}{3}} z^{-\frac{1}{3}}, \quad B = \frac{5}{6\alpha_u}\left[\frac{5}{9\alpha_u}\left(\frac{2F_0}{\pi}\right)^2\right]^{\frac{1}{3}} z^{-\frac{5}{3}}. \tag{16}$$

The predicted plume envelope $R(z)$, shown in Figure 2 with black dashed lines, matches the passive tracer distribution shown by shading. The predicted w and b profiles, shown in Figure 3a (dashed curves, below the red dashed line that marks the interface), also match the simulated w and b, which are shown by solid curves. Generally speaking, MTT prediction captures the behaviors of a non-rotating plume, as have been found in previous studies (e.g., List, 1982; Rouse et al., 1952; Wang et al., 2025).

In a stratified environment ($N \neq 0$), the MTT model (Equations 10–12) can only be solved numerically. Also, because the w and b horizontal profile deviate from the Gaussian form (Equation 14), as can be seen in Figure 3c, a "top-hat" distribution is perhaps more appropriate for w and b (Morton, 1959). This change gives rise to the geometric factor $\xi = 1$ instead of $\sqrt{2}$. Lab experiments have estimated the entrainment coefficient α_n (the subscript "n" denotes the stratified case) to be around 0.116 instead of 0.093 (Morton, 1959). We adopt these coefficients and numerically integrate the MTT model (Equations 10–12) beyond the stratification interface, using the final values of R, W, and B in the unstratified layer as initial conditions (Equation 16). The resulting vertical profiles show close agreement with our simulations for $\hat{z} \geq 5$ (above the red dashed line in Figure 3a), capturing the decrease and eventual reversal of b as well as the decay of w to zero at the terminal height.

However, as shown in Figure 3a, some discrepancies between the simulation results and the MTT predictions can be noted near the bottom boundary. The MTT model predicts that w and b tend to infinity, while the simulated w is smaller and b is larger. These discrepancies stem from the presences of a bottom boundary in the simulation, which does not exist in the MTT model. We also note that the finite size of the source may introduce additional discrepancies, which can be addressed by introducing a virtual origin beneath the source (Hunt & Kaye, 2001; Tarshish & Romps, 2022). However, this does not help address the discrepancies in our simulations. Furthermore, in a stratified environment, the MTT model describes only the rising plume core and does not capture the outer sinking flow that occurs beyond the neutral buoyancy level. Because of this reason, the MTT model predicts that

the plume radius R becomes infinite when M approaches zero. These limitations are addressed by recognizing the formation of a double-plume structure, that is, an inner rising plume surrounded by an outer sinking annular plume (McDougall, 1981). Despite these limitations, the MTT model adequately predicts the bulk centerline profiles of w and b and suffices to predict the plume terminal height, as shown subsequently.

4.2. Plume Terminal Height

In this section, we attempt to quantify the terminal height of the plume h_w, or equivalently, the penetration height $z_p \equiv h_w - h_i$, since it determines how far heat and materials can be transported. Specifically, we would like to derive a scaling law for h_w and z_p, which would obviate the need to solve the MTT model and develop a deeper understanding of the factors that control the penetration height.

To diagnose the terminal height h_w, for each of our simulations, we track the temporal evolution of the plume height h_p, which is defined as the maximum height of the contour $c/c_s = 10^{-4}$, and we compute the average of h_p after the growth of h_p plateaus. The resulting terminal height $\hat{h}_w$ and penetration height $\hat{z}_p$ are shown in Figure 4 as functions of $\hat{h}_i$, after nondimensionalized by L_N.

When $\hat{h}_i \leq 1$, corresponding to a thin—or, in extreme cases, absent—unstratified lower layer, the dilution of the plume within this layer is negligible, allowing the plume to retain its potential to penetrate deeply into the stratified region. In this case, the penetration depth $\hat{z}_p$ scales linearly with L_N, with a prefactor of ~4.76, consistent with previous measurements in uniformly stratified environments (Devenish et al., 2010; Morton et al., 1956; Turner, 1973; W. Zhang et al., 2017).

When $\hat{h}_i > 1$, corresponding to a higher interface, a weaker buoyancy source, or stronger stratification, dilution in the lower layer can significantly reduce the penetration potential of the plume. Consequently, $\hat{z}_p$ decreases following a best-fit scaling of $4.25\hat{h}_i^{-1/3}$ (Figure 4b). These results are consistent with previous studies of plumes in partially stratified environments (Ansong & Sutherland, 2010; Powell, Sutherland, et al., 2025), whose measurements are also compiled in Figure 4.

The two scaling laws in the low limit $\hat{h}_i$ and the high limit $\hat{h}_i$ can be derived from the MTT model. In the stratified layer, Equations 10–12 cannot be solved analytically, so we use the "unaltered volume flux" technique, where it is assumed that vertical volume flux Q remains close to the unstratified solution (Equation 15). This approach can be justified through an asymptotic analysis, which was detailed in Briggs (1982), Scase et al. (2006), and Devenish et al. (2010). Substituting Q in Equation 15 into Equations 11 and 12 and integrating them to z, we get

$$F = F_i - \frac{3}{8}CN^2\left(z^{\frac{8}{3}} - h_i^{\frac{8}{3}}\right), \tag{17}$$

$$M = \left[M_i^2 - \frac{9}{64}C^2N^2\left(z^{\frac{8}{3}} - h_i^{\frac{8}{3}}\right)^2 + \frac{3}{4}CF_i\left(z^{\frac{8}{3}} - h_i^{\frac{8}{3}}\right)\right]^{\frac{1}{2}}, \tag{18}$$

where F_i and M_i are the buoyancy and momentum fluxes evaluated at the interface from Equation 15, and $C = \frac{6\pi\alpha_u}{5}\left(\frac{18\alpha_u}{5\pi}\right)^{\frac{1}{3}}F_0^{\frac{1}{3}}$. The terminal height h_w corresponds to the level where $M = 0$, which follows

$$\hat{h}_w = \left\{\hat{h}_i^{\frac{8}{3}} + \left(\frac{20}{9\alpha_u}\right)^{\frac{4}{3}}\pi^{-\frac{2}{3}}\left[1 + \sqrt{1 + 4\left(\frac{9\alpha_u}{20}\right)^{\frac{4}{3}}\pi^{\frac{2}{3}}\hat{h}_i^{\frac{8}{3}}}\right]\right\}^{\frac{3}{8}}. \tag{19}$$

For the limit of the thin unstratified lower layer $(\hat{h}_i \to 0)$, this scaling reduces to

$$\hat{h}_w \approx 2^{\frac{3}{8}}\left(\frac{20}{9\alpha_u}\right)^{\frac{1}{2}}\pi^{-\frac{1}{4}} \approx 4.76. \tag{20}$$

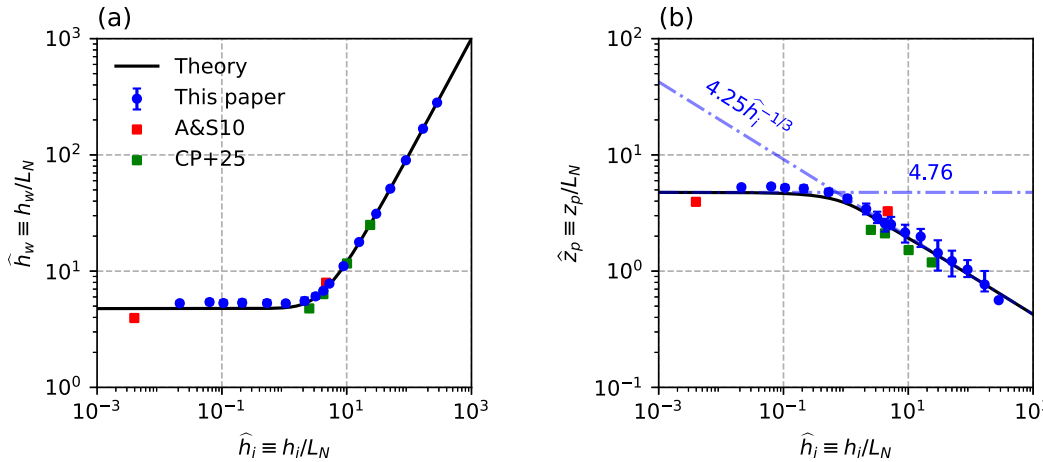

Figure 4. Relations between the dimensionless interface height $\hat{h}_i$ and (a) the terminal height $\hat{h}_w$, and (b) the penetration height $\hat{z}_p$, for plumes in the non-rotating regime. Black curves are theoretical predictions from Equation 19. Blue dots denote results from simulations listed in the upper portion of Table 1, with error bars indicating the maximum and minimum values over the evaluation interval. Red and green squares show results from Ansong and Sutherland (2010), labeled A&S10, and Powell, Sutherland, et al. (2025), labeled CP+25, respectively. In panel (b), the blue dash-dotted lines represent the asymptotic limits given by Equations 20 and 21.

For the limit of the thick unstratified layer ($\hat{h}_i \gg 1$), $\hat{h}_w$ is approximated as

$$\hat{h}_w \approx \hat{h}_i + \frac{3}{4}\left(\frac{20}{9\alpha_u}\right)^{\frac{2}{3}} \pi^{-\frac{1}{3}} \hat{h}_i^{-\frac{1}{3}} \approx \hat{h}_i + 4.25\hat{h}_i^{-\frac{1}{3}}. \tag{21}$$

These scalings are shown in Figure 4 and quantitatively agree with the best-fit scaling for our simulations and previous studies.

5. Point Plumes in the Rapid-Rotating Regime

5.1. Plume Evolution

The fate of a rotating penetrative plume differs markedly from that in the non-rotating regime. Snapshots of rotational simulations are shown in Figure 5. Unlike the non-rotating case (Figure 2), the plume envelope no longer follows a cone shape.

During the early evolution, the plume first develops a cone-like shape similar to the non-rotating case. Then, as the radius of the plume expands and w decreases, the Rossby number $Ro \equiv \frac{w}{fR}$ drops, indicating that rotation becomes more important. When $Ro < 1$, the Coriolis force deflects the entrained inflow into a rim current around the plume, inhibiting further entrainment. Consequently, lateral expansion is suppressed and the plume transits from a cone to a cylindrical shape. The transition height h_c between the cone and the cylinder and the radius of the cylinder r_c scale as

$$h_c \approx 6L_{\text{rot}}, \quad r_c \approx L_{\text{rot}}, \tag{22}$$

as seen in the left column of Figure 5. This agrees with previous laboratory experiments (Fernando et al., 1998; Goodman et al., 2004) and numerical simulations (Wang et al., 2025). In addition, Equation 22 is used to identify the rapid-rotating regime (Figure 1c), that is, $h_i > h_c$, where the plume is rotation-dominated before reaching the interface.

However, the cylindrical plume is short-lived as it is deformed by the boundary transport near the surface (Figure 5). This reduces the plume width near the source, forming a tornado-like shape (Figure 5b), as described by Sutherland et al. (2021), and the tornado plume precesses around the direction of gravity as a gyroscope driven by buoyancy force and adverse pressure force (Fabregat Tomàs et al., 2016; Frank et al., 2017). This precession

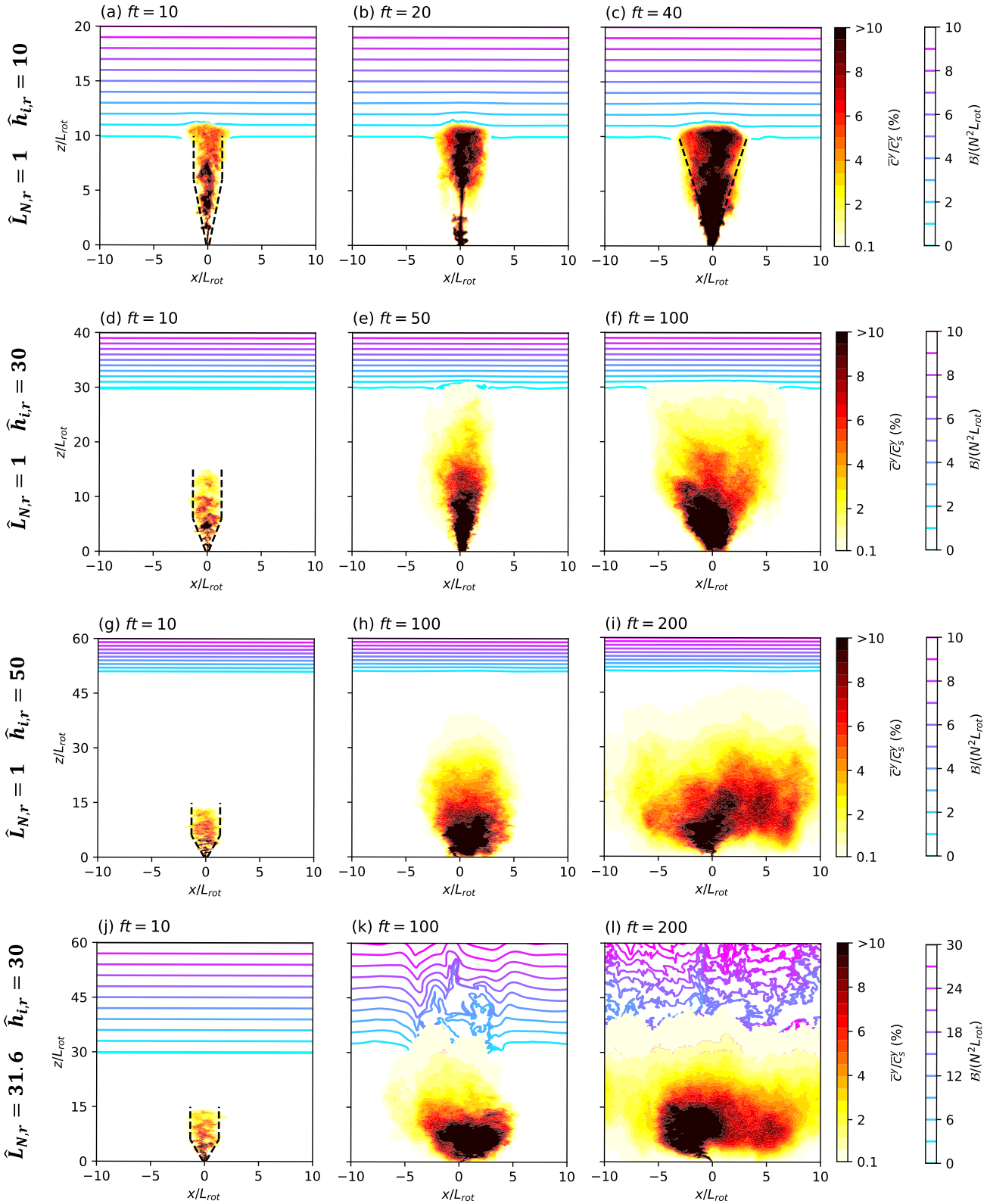

Figure 5.

makes the plume appears wider than it actually is (Figure 5e). Subsequently, baroclinic or barotropic instabilities onset, as rim current strengthens. The generated eddies break the primary plume into secondary plumes (Figures 5f, 5h, 5i, 5k, and 5l) and export momentum and buoyancy laterally (Bire et al., 2023; Wang et al., 2025; Whitehead et al., 1996).

Whether the plume has already undergone significant re-expansion upon reaching the interface depends on how far along it has evolved in the lower layer, as measured by the interface height h_i nondimensionalized by L_{rot} (denoted as $\hat{h}_{i,r}$). For $\hat{h}_{i,r}$ less than 20, the cylindrical structure persists into the stratification (Figures 5a and 5b). Otherwise, the cylinder breaks down and spreads extensively in the radial direction before impingement (e.g., Figure 5e). In an extreme regime where $\hat{h}_{i,r} > 50$, the plume breaks down significantly and fails to reach the stratified layer, instead stalling at a certain height below the interface (e.g., Figure 5i). This phenomenon has also been observed in unstratified environments in previous studies (Bire et al., 2023; Goodman et al., 2004; Wang et al., 2025), and is explained by the onset of baroclinic instabilities (Wang et al., 2025).

If the rotating plume is able to reach the interface, its post-penetration evolution also differs markedly from that in the non-rotating regime. When stratification is strong ($N \geq f$, or equivalently $\hat{L}_{N,r} \leq 1$), the post-penetration evolution resembles that of a plume impinging on a rigid surface (Fernando et al., 1998; Goodman et al., 2004; Wang et al., 2025). The subsidence of the fluid from the terminal to the neutral height is barely observed (Figures 5c and 5f). As a result, the fluid intrudes near the terminal height close to the interface, forming a flat plume cap. Moreover, instead of the "mushroom" structure in the non-rotating case (Figure 2c), this rotating plume develops into a baroclinic cone (Figure 5c), as outward flows in the intrusion layer are deflected into anticyclonic currents, leading to mass accumulation and lateral spreading throughout the plume. The diameter of this cone scales with the deformation radius of a two-layer fluid (Goodman & Lenferink, 2012; Goodman et al., 2004; Pedlosky, 1987),

$$L_{\text{cone}} = \frac{\sqrt{bh_i}}{f} \sim \sqrt{L_{\text{rot}} h_i}, \tag{23}$$

as shown in Figure 5c. Ultimately, baroclinic instabilities fragment the primary cone into multiple secondary plumes that drift outward, resembling the behavior of plumes impinging on a rigid surface (Fernando et al., 1998; Goodman et al., 2004). This stage is not shown here as it does not affect the penetration depth.

In contrast, if the rotating plume cannot reach the interface height ($\hat{h}_{i,r} > 50$), or similarly, if stratification is much weaker than rotation ($N \ll f$, or equivalently $\hat{L}_{N,r} \gg 1$), the evolution of the plume is hardly influenced by stratification (Figures 5i and 5l). The plume undergoes baroclinic instabilities and spreads horizontally at $\sim 50 L_{\text{rot}}$.

5.2. Plume Terminal Height

The penetration of the plume can be measured by the terminal height $\hat{h}_{w,r}$, or equivalently, the penetration height $\hat{z}_{p,r}$ that subtracts $\hat{h}_{i,r}$ from $\hat{h}_{w,r}$. In Figure 6b, $\hat{z}_{p,r}$ is presented for all our simulations, as a function of $\hat{h}_{i,r}$ for various $\hat{L}_{N,r}$ (indicated by different colors). As $\hat{h}_{i,r}$ decreases, $\hat{z}_{p,r}$ increases and asymptotically approaches a constant that depends on $\hat{L}_{N,r}$. This trend can be understood as follows.

In the limit of low $\hat{h}_{i,r}$, the plume retains the cylindrical structure upon impinging the interface (e.g., Figure 5a). Within the cylindrical structure, w and b hardly vary with height z (Goodman et al., 2004; Wang et al., 2025). Therefore, as long as the stratification interface falls in the range of nearly uniform w and b, the initial momentum and buoyancy fluxes of the plume are fixed, giving rise to a nearly constant $\hat{z}_{p,r}$ (Figure 6b).

Figure 5. Same as Figure 2, but for simulations in the rapid-rotating regime listed in Table 1. Panels (a–i) correspond to $\hat{L}_{N,r} = 1$ (strong stratification) and panels (j–l) to $\hat{L}_{N,r} = 31.6$ (weak stratification). Color shading shows the dimensionless $y-$averaged tracer concentration $\overline{c}^y/\overline{c}^y_s$. The interface between the unstratified and stratified layers is located at $\hat{h}_{i,r} = 10$ in panels (a–c), $\hat{h}_{i,r} = 30$ in (d–f), $\hat{h}_{i,r} = 50$ in (g–i), and $\hat{h}_{i,r} = 30$ in (j–l). In the left column and in panel (c), black dashed lines represent boundaries of the cylindrical plume (Equation 22) and baroclinic cone (Equation 23), respectively.

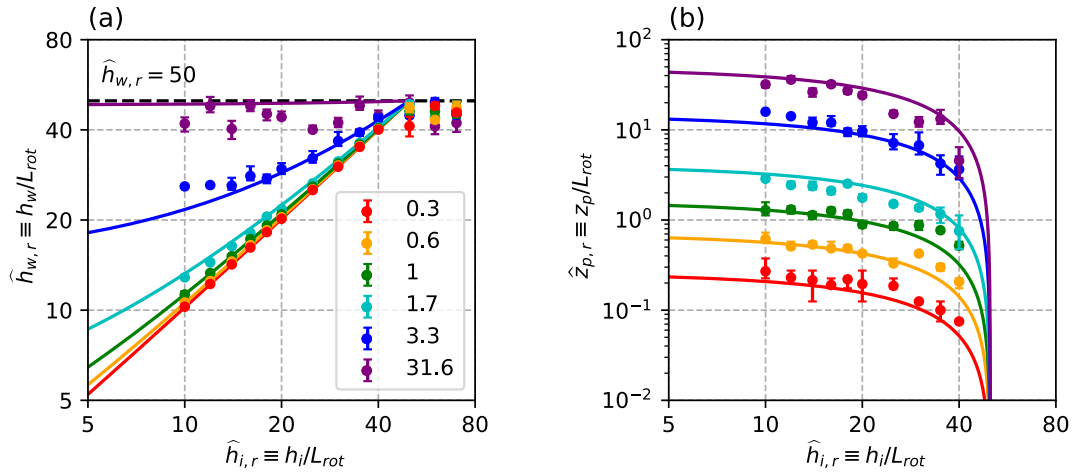

Figure 6. Same as Figure 4, but for the rapid-rotating regime, where all heights are scaled by $L_{\rm rot}$. In panel (a), the black dashed line represent the upper limit $\hat{h}_{w,r} = 50$. Colored curves are theoretical predictions from Equation 32 for different values of $\hat{L}_{N,r} \equiv L_N/L_{\rm rot}$. Colored dots represent simulation results with corresponding $\hat{L}_{N,r}$ values listed in lower portion of Table 1.

In the limit of high $\hat{h}_{i,r}$, as discussed in Section 5.1, baroclinic instability would scatter the momentum and buoyancy away from the source, preventing the plume height from exceeding $\hat{h}_{w,r} \sim 50$ (Figure 6a). Therefore, if $\hat{h}_{i,r} > 50$, the plume will stop growing before reaching the interface (Goodman et al., 2004; Wang et al., 2025). In this circumstance, the penetration height $\hat{z}_{p,r}$ becomes ill-defined, and instead we use the terminal height $\hat{h}_{w,r}$ to measure the penetration. As can be seen in Figure 6a, $\hat{h}_{w,r}$ increases with $\hat{h}_{i,r}$ and saturates at $\hat{h}_{w,r} = 50$ as predicted.

Another trend shown in Figure 6 is that plume penetration, measured by both $\hat{h}_{w,r}$ and $\hat{z}_{p,r}$, tends to increase monotonically with $\hat{L}_{N,r}$. This is not surprising, as the greater $\hat{L}_{N,r}$ corresponds to a weaker stratification and therefore a deeper penetration of the plume.

Here we derive a scaling law for the terminal height $\hat{h}_{w,r}$. Following the approach in Section 4.1, we write the governing equations for the vertical fluxes of volume Q, momentum M, and buoyancy F as

$$\frac{\mathrm{d}Q}{\mathrm{d}z} = -2\pi r_p u^*, \tag{24}$$

$$\frac{\mathrm{d}M}{\mathrm{d}z} = \frac{FQ}{M} - P - 2\pi r_p u^* w_p, \tag{25}$$

$$\frac{\mathrm{d}F}{\mathrm{d}z} = -N^2 Q - 2\pi r_p u^* b_p. \tag{26}$$

Here, r_p is the radius of the cylindrical plume, w_p and b_p are the characteristic vertical velocity and buoyancy within the plume, u^* is an effective radial velocity representing eddy-driven lateral transport, and P denotes the work performed by the adverse vertical pressure gradient,

$$P \equiv \iint \frac{\partial p}{\partial z} r \mathrm{d}r\mathrm{d}\theta, \quad p \approx \int (fv)\,\mathrm{d}r, \tag{27}$$

where v is the azimuthal velocity.

These equations differ from the non-rotating MTT model (Equations 10–12) in two essential ways. First, growth in Q due to entrainment is suppressed by rotation (Fernando et al., 1998; Goodman et al., 2004). Instead, baroclinic instabilities fragment the plume and drive lateral leakage of volume, momentum, and buoyancy, parameterized by the fluxes u^*, $u^* w_p$, and $u^* b_p$, respectively. Second, the establishment of the rim current

produces a pressure anomaly at the core of the plume, generating an adverse pressure gradient that partially offsets buoyant acceleration. This effect is represented by P. In contrast, in the non-rotating regime, P is negligible compared to the buoyancy work FQ/M (Morton et al., 1956).

Since the stratification assumed here, N, is a piecewise linear function of z, we integrate Equations 24–26 separately within the unstratified and stratified regions to obtain analytical solutions for Q, M, and F, from which the terminal height $\hat{h}_{w,r}$ is determined by identifying the height where M vanishes.

In the unstratified region, the rim current satisfies the thermal-wind balance (Figure S1 in Supporting Information S1; also see Fernando et al., 1998; Goodman & Lenferink, 2012; Goodman et al., 2004), that is,

$$\frac{\partial v}{\partial z} = \frac{1}{f}\frac{\partial b}{\partial r}. \tag{28}$$

Substituting this relation into Equation 27, one can find that FQ/M is largely compensated by P (see Figure S1 in Supporting Information S1), in accordance with Fabregat Tomàs et al. (2016). Dropping FQ/M and P and substituting $N = 0$, Equations 24–26 reduce to

$$\frac{\mathrm{d}Q}{\mathrm{d}z} = -2\pi r_p u^*, \quad \frac{\mathrm{d}M}{\mathrm{d}z} = -2\pi r_p u^* w_p, \quad \frac{\mathrm{d}F}{\mathrm{d}z} = -2\pi r_p u^* b_p. \tag{29}$$

These equations can be closed once u^* is specified. Based on numerical simulations from Legg et al. (1996) and Visbeck et al. (1996), we parameterize $u^* = \gamma \Delta v_{\mathrm{rim}}$, where $\gamma \approx 0.25$ is a constant and Δv_{rim} is the vertical shear of the rim current across the plume, estimated from the thermal-wind relation (Equation 28). Substituting this closure, we obtain the following solutions (see Supporting Information S1 for details),

$$Q = Q_0\left(1 - \frac{z}{50L_{\mathrm{rot}}}\right), \quad M = M_0\left(1 - \frac{z}{50L_{\mathrm{rot}}}\right)^2, \quad F = F_0\left(1 - \frac{z}{50L_{\mathrm{rot}}}\right)^2, \tag{30}$$

where Q_0 and M_0 are the volume and momentum fluxes achieved during the non-rotating (MTT) phase (Goodman et al., 2004). These solutions imply a terminal height

$$\hat{h}_{w,r} \approx 50 \tag{31}$$

in an unstratified ocean, consistent with simulations at very large interface heights (e.g., Figure 5i) and with previous studies (Bire et al., 2023; Wang et al., 2025).

For the stratified region, we need to make two different approximations. First, we assume that the baroclinic dilution remains at the same level as in the unstratified case. Furthermore, when entering a strongly stratified region, the thermal-wind balance (Equation 28) cannot be immediately restored, so the magnitude of P becomes smaller than that of FQ/M (Fabregat Tomàs et al., 2016). As the buoyancy becomes negative beyond the neutral buoyancy level, the plume will decelerate not only by baroclinic dilution (3rd term in the RHS of Equation 25), but also by buoyancy force (1st term in the RHS of Equation 25). To make the equations analytically tractable, we solve Equation 25 with only the dilution term $2\pi r_p u^* w_p$ or only the buoyancy work FQ/M, and choose the smaller one as the final solution. Keeping only the dilution term, we rediscover the solution for the unstratified region (Equation 31). Keeping the buoyancy term, we obtain the following.

$$\hat{h}_{w,r} = \hat{h}_{i,r} + \frac{0.35\hat{L}_{N,r}^{\frac{8}{3}}}{1 + 0.015\hat{L}_{N,r}^{\frac{8}{3}}}\left(1 - \frac{\hat{h}_{i,r}}{50}\right)\left(1 + \sqrt{1.18 + 12.3\hat{L}_{N,r}^{-\frac{8}{3}}}\right). \tag{32}$$

Detailed deviations are provided in Supporting Information S1. Since this solution always predicts a smaller terminal height than in the unstratified case, it is chosen as the final solution.

The predicted $\hat{h}_{w,r}$ (Equation 32) is plotted in Figure 6 for various $\hat{L}_{N,r}$, denoted by different colors, and they match our simulations reasonably well.

6. Implications for Icy Satellites

Hydrothermal plumes are believed to exist in the subsurface oceans of Europa, Enceladus, and potentially Titan (as long as the subsurface ocean interacts with the rocky core), delivering heat and materials from the seafloor to the ice shell (Bire et al., 2023; Collins et al., 2000; Goodman et al., 2004; Thomson & Delaney, 2001). However, their ascent may be limited by a stably stratified layer in the upper ocean, which arises from the pressure dependence of the freezing point and associated temperature variations induced by spatial variations in ice thickness (Figure 1a; Kang, Mittal, et al., 2022; Lobo et al., 2021; Y. Zhang et al., 2024). Applying our scaling relations (Equations 19 and 32), we can estimate how deeply hydrothermal plumes penetrate into the ocean and assess whether they can reach the ice shell. The key parameters in the scaling, the hydrothermal buoyancy flux F_0, the Coriolis parameter f, the stratification strength N and the interface height h_i, are estimated as follows:

- The source buoyancy flux F_0 is given by

$$F_0 = \frac{g\alpha_T \mathcal{H}}{\bar{\rho}_w c_p}, \tag{33}$$

  where g is gravity, α_T is thermal expansivity, $\mathcal{H}$ is hydrothermal heat flux, $\bar{\rho}_w$ is the reference potential density of water, and c_p is the heat capacity of water.
- The Coriolis parameter $f = 2\Omega$, where Ω is the moon's rotation rate, as we focus on the polar region.
- Since the temperature along the ice–ocean interface follows the freezing point T_f, which decreases with depth, the upper ocean is expected to be stratified, as sketched in Figure 1a. The temperature (buoyancy) drop across the stratified layer, ΔT, follows

$$\Delta T = \Delta T_f = a_0 \Delta p_{\text{ice}} = a_0 \rho_i g \Delta D_{\text{ice}}, \tag{34}$$

  where $a_0 = -7.61 \times 10^{-8}$ K Pa^{-1}, ρ_i is the density of ice, and ΔD_{ice} is the spatial variation (large-scale) of the thickness of the ice. The buoyancy frequency in this layer, N, which scales the strength of the stratification, is then determined as

$$N = \sqrt{-\frac{g\alpha_T \Delta T}{D_{\text{layer}}}}, \tag{35}$$

  where D_{layer} is the thickness of the stratified layer.

  As long as $\alpha_T > 0$, which generally holds unless the salinity of the ocean is very low and the size of the satellite is small, the stratification is set by the balance between the downward heat diffusion and the upward heat advection by ocean dynamics. Y. Zhang et al. (2024) provides an analytical framework to compute D_{layer} and thereby the stratification N. D_{layer} increases with vertical diffusivity κ by molecular diffusion and tidal mixing, and decreases with ice thickness difference ΔD_{ice}. When $\kappa \to 0$ or ΔD_{ice} is large enough, D_{layer} approaches ΔD_{ice}, and N reaches its maximum value.
- The interface height h_i is estimated as

$$h_i = D_{\text{ocn}} - D_{\text{layer}}, \tag{36}$$

  where D_{ocn} is the thickness of the ocean (in the polar region).

To compute the heat flux $\mathcal{H}_c$ needed for a point plume to reach the upper surface, we take the following steps. We first set the terminal height h_w equal to the thickness of the ocean D_{ocn}, and separately compute $\mathcal{H}_c$ based on Equations 19 and 32. This procedure yields two values of $\mathcal{H}_c$, but only one is physically valid. To select the physical solution, we compute $\hat{h}_{i,r}$ for each $\mathcal{H}_c$ and use the fact that the rotation-dominant formula (Equation 32) requires $\hat{h}_{i,r} > 6$, whereas the non-rotating formula (Equation 19) requires the opposite.

Figure 7 shows $\mathcal{H}_c$ for Europa, Enceladus, and Titan, as a function of the thickness of the ocean D_{ocn} and the variation of the thickness of the ice ΔD_{ice}. The plausible ranges of D_{ocn} and ΔD_{ice} inferred from the observations

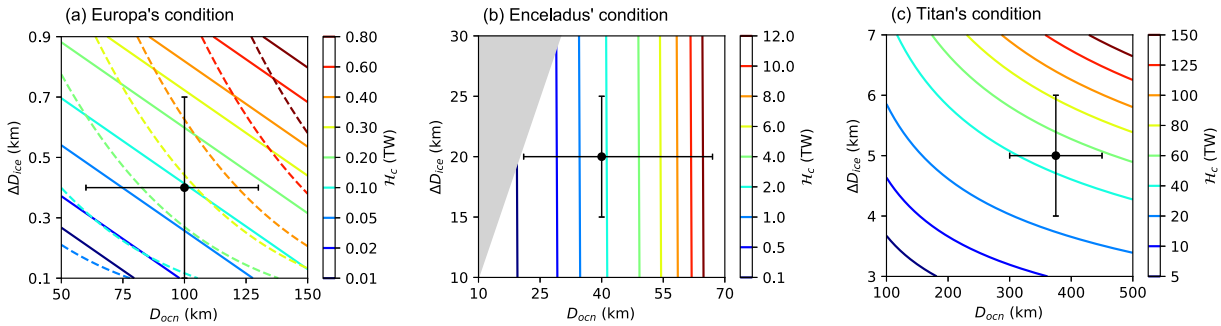

Figure 7. Predicted critical hydrothermal heat fluxes $\mathcal{H}_c$ required for plumes in the polar region to reach the ice shell under the conditions for (a) Europa, (b) Enceladus, and (c) Titan, based on Equations 19 and 32. Solid curves correspond to cases where the thickness of the stratified layer D_{layer} equals to ΔD_{ice} (horizontal isopycnals); dashed curves correspond to D_{layer} for tilted isopycnals, calculated following Y. Zhang et al. (2024). In panels (b) and (c), the two groups of curves overlap because D_{layer} is close to ΔD_{ice}. The likely positions for Europa, Enceladus, and Titan are marked by black dots in each panel. The gray shading in panel (b) represent invalid parameter regime where the ocean depth is smaller than the ice thickness variation.

are also marked in the plots. The parameters used in the calculation are summarized in Table 2. Among the three satellites considered, Europa has the smallest $\mathcal{H}_c$, on the order of 10–100 GW. Since this value is lower than the total heat production rate on Europa (~1000 GW), plume penetration is possible. In contrast, for plumes to penetrate the oceans of Enceladus and Titan, the minimum required heat fluxes are ~100 GW and ~5,000 GW, respectively. These values far exceed the total heat production in these satellites, making plume penetration impossible. Similar results have been reported by Bire et al. (2023) and Wang et al. (2025) for Enceladus. On Enceladus, this is primarily because its small gravity and thermal expansion coefficient, combined with rapid rotation, lead to a very small L_{rot}. Moreover, as $N \ll f$ on Enceladus, the critical heat flux $\mathcal{H}_c$ only depends on the ocean depth, that is, $D_{\text{ocn}} \approx 50 L_{\text{rot}}$ (Figure 7b). On Titan, by contrast, convective plumes are inhibited from reaching the surface because of the large N under its thin polar ice induced by the ice thickness variations. Broadly speaking, it is more difficult for a plume to reach the ice shell on an icy satellite that features larger ice thickness variation, smaller gravity, and faster rotation.

Table 2
Estimated Parameter Values for Europa, Enceladus and Titan

Name	Symbol (Units)	Europa	Enceladus	Titan
Planetary parameters				
Gravity	g (m s^{-2})	1.315	0.113	1.352
Rotation rate	Ω (s^{-1})	2.1×10^{-5}	5.3×10^{-5}	4.6×10^{-6}
Radius	R (km)	1,561	252	2,575
Ocean thickness	D_{ocn} (km)	60 ~ 130[a]	21 ~ 67[a]	300–450[a]
Ice thickness variation	ΔD_{ice} (km)	≤ 1[b]	15 ~ 25[b]	4 ~ 6[b]
Physical parameters				
Ice density	ρ_i (kg m^{-3})		917	
Water density	$\bar{\rho}_w$ (kg m^{-3})		1,000	
Water heat capacity	c_p (J kg^{-1} K^{-1})		4,000	
Vertical diffusivity	κ (m^2 s^{-1})		≥ 10^{-6}	
Thermal expansivity	α_T (K^{-1})	3×10^{-4}[c]	1×10^{-5}[c]	3×10^{-4}[c]

[a]Ref: Europa (Anderson et al., 1998; Billings & Kattenhorn, 2005; Nimmo et al., 2007; Soderlund, 2019; Soderlund et al., 2020; S. D. Vance et al., 2018); Enceladus (Beuthe et al., 2016; Hoolst et al., 2016; Iess et al., 2014; Soderlund et al., 2020; Thomas et al., 2016); Titan (MacKenzie et al., 2021; Soderlund et al., 2020). [b]Ref: Europa (Kang, 2022; Nimmo et al., 2007); Enceladus (Beuthe et al., 2016; Čadek et al., 2016; Hemingway & Mittal, 2019); Titan (Lefevre et al., 2014; Soderlund et al., 2020). [c]Ref: (Bire et al., 2022, 2023; Soderlund, 2019).

It should be noted that $\mathcal{H}_c$ in Figure 7 is an optimistic estimate. First, we use $\kappa = 10^{-6}$ m^2 s^{-1}, which is molecular diffusivity and corresponds to minimum D_{layer}. However, considering tidal mixing, κ can increase several orders, making D_{layer} much thicker and hence large $\mathcal{H}_c$ for the plume to penetrate. Second, we do not account for the additional stratification induced by salinity. Assuming the ice shell is close to steady state, equatorial freezing and polar melting are required to maintain poleward-thinning ice geometry against ice flow (Ashkenazy et al., 2018). This implies that the water beneath the equatorial ice is likely to be saltier than the water beneath the polar ice. Such salinity contrasts add to the density variation induced by the sub-ice temperature gradient, further enhancing stratification N and suppressing plume penetration. Furthermore, on small icy moons, such as Enceladus, water can contract upon warming at low salinity. In this case, convection will be completely suppressed, at least near the ice–ocean interface, if not throughout the entire column (Kang, Marshall, et al., 2022; Zeng & Jansen, 2021). This scenario is beyond the scope of our present work and needs to be investigated separately.

7. Summary and Discussion

We have investigated the evolution of point plumes in a partially stratified environment composed of a lower unstratified layer overlain by a linearly stratified layer (Figure 1a), with implications for subsurface oceans on icy satellites. Our main focus is on the plume penetration height.

The fate of the plume in this system is fully cataloged in a one-dimensional parameter space spanned by $\hat{h}_i \equiv h_i/L_N$ for the non-rotating regime (Figure 1b) and a two-dimensional parameter space spanned by nondimensional numbers $\hat{L}_{N,r} \equiv L_N/L_{\text{rot}}$ and $\hat{h}_{i,r} \equiv h_i/L_{\text{rot}}$ for the rotating regime (Figure 1c). Here, h_i is the height of the interface between the unstratified and stratified layers, and $L_N \equiv \left(F_0/N^3\right)^{1/4}$ and $L_{\text{rot}} \equiv \left(F_0/f^3\right)^{1/4}$ are two characteristic length scales, where F_0 is the buoyancy flux of source, N is the buoyancy frequency, and f is the Coriolis parameter. This work focuses on the non-rotating regime and the rapid-rotating regime ($\hat{h}_{i,r} > 6$), the latter of which has not been explored by previous works.

In the non-rotating regime, the plume rises as a cone in the unstratified layer (Figure 2a), impinges on the interface at $z = h_i$, overshoots due to inertia (Figure 2b), and eventually subsides and intrudes laterally, forming a classical "mushroom" structure (Figure 2c). The structure and dynamics are well captured by the MTT model (Equations 10–12 and Figure 3; also see Morton et al., 1956). In this regime, we propose a scaling law for the penetration height of the plume z_p (Equation 19). When the interface lies close to the source, the scaling gives a constant $z_p \approx 4.76L_N$. When the interface h_i is higher than L_N, the penetration weakens and follows $z_p = 4.25h_i^{-\frac{1}{3}}L_N^{\frac{4}{3}}$ (Figure 4).

In the rapid-rotating regime, the plume likewise begins as a MTT cone in the unstratified layer, but rotation soon suppresses entrainment and the plume transitions to a vertically coherent, nearly cylindrical shape with almost constant fluxes (Figures 5a, 5d, 5g, and 5j). In an unstratified environment, the plume can reach a maximum height $\sim 50L_{\text{rot}}$ before being completely disrupted and scattered by baroclinic eddies, consistent with previous studies (Bire et al., 2023; Goodman et al., 2004; Wang et al., 2025). This means that if the height of the interface h_i is greater than $50L_{\text{rot}}$, the plume will not even reach the stratified layer, let alone the top of the domain (Figure 5i). If $h_i < 50L_{\text{rot}}$, then the plume can reach the interface, and the terminal height of the plume h_w will be further reduced by stratification N following Equation 32 as shown by Figure 6.

Applying these scalings to the polar oceans of Europa, Enceladus, and Titan allows us to assess the likelihood that hydrothermal plumes will reach the ice shell. Due to the strong variations in the thickness of the ice on Enceladus and Titan, the hydrothermal heat flux required for a plume to reach the base of the ice, $\mathcal{H}_c$, is greater than 100 GW and 5,000 GW, respectively (Figures 7b and 7c), far greater than the total heat production of the moons! Therefore, direct plume-mediated transport to the ice shell appears implausible there, in agreement with previous studies (Bire et al., 2023; Wang et al., 2025). On Europa, on the contrary, larger gravity and weaker rotation act together to confine plumes to larger scales, so that plume penetration to the ice shell is feasible, with $\mathcal{H}_c$ ranging from several to hundreds of GW depending on ocean depth and ice-thickness variations (Figure 7b).

We note that the above analysis assumes a positive thermal expansivity α_T. However, on small icy moons such as Enceladus, α_T can become negative when the mean salinity is low (S. Vance et al., 2009). In this case, convection cannot be triggered by basal heating unless the temperature exceeds several degrees Celsius, where the water

reaches its maximum density (Bire et al., 2023; Kang, Marshall, et al., 2022; Zeng & Jansen, 2021), making the present analysis inapplicable. In addition, our discussion has been limited to plumes beneath the polar regions. At lower latitudes, the planetary rotation vector is no longer aligned with gravity, giving rise to fundamentally different flow regimes, as discussed by previous studies (Aurnou et al., 2003; Bire et al., 2022; Busse, 1970; Gastine et al., 2016; Soderlund, 2019).

Conflict of Interest

The authors declare no conflicts of interest relevant to this study.

Availability Statement

The data analyzed in the present study are produced by *Oceananigans.jl* (Ramadhan et al., 2020) and are available at Wang (2025).

Acknowledgments
The authors thank Ali Ramadhan, Simone Silvestri, Gregory L. Wagner, and Xin Kai Lee for technical support for Oceananigans, the MIT Satori Group and the Svante Group for support with computing resources, Cheng Li for helpful discussion, and Jason Goodman for insightful comments. WK acknowledges support from startup funding. JM acknowledges support from NASA Astrobiology Grant 80NSSC19K1427 "Exploring Ocean World".

References

Anderson, J. D., Schubert, G., Jacobson, R. A., Lau, E. L., Moore, W. B., & Sjogren, W. L. (1998). Europa's differentiated internal structure: Inferences from four Galileo encounters. *Science*, *281*(5385), 2019–2022. https://doi.org/10.1126/science.281.5385.2019

Ansong, J. K., & Sutherland, B. R. (2010). Internal gravity waves generated by convective plumes. *Journal of Fluid Mechanics*, *648*, 405–434. https://doi.org/10.1017/S0022112009993193

Ashkenazy, Y., Sayag, R., & Tziperman, E. (2018). Dynamics of the global meridional ice flow of Europa's icy shell. *Nature Astronomy*, *2*(1), 43–49. https://doi.org/10.1038/s41550-017-0326-7

Aurnou, J., Andreadis, S., Zhu, L., & Olson, P. (2003). Experiments on convection in earth's core tangent cylinder. *Earth and Planetary Science Letters*, *212*(1), 119–134. https://doi.org/10.1016/S0012-821X(03)00237-1

Beuthe, M., Rivoldini, A., & Trinh, A. (2016). Enceladus's and Dione's floating ice shells supported by minimum stress isostasy. *Geophysical Research Letters*, *43*(19), 10088–10096. https://doi.org/10.1002/2016GL070650

Billings, S. E., & Kattenhorn, S. A. (2005). The great thickness debate: Ice shell thickness models for Europa and comparisons with estimates based on flexure at ridges. *Icarus*, *177*(2), 397–412. https://doi.org/10.1016/j.icarus.2005.03.013

Bire, S., Kang, W., Ramadhan, A., Campin, J.-M., & Marshall, J. (2022). Exploring ocean circulation on icy moons heated from below. *Journal of Geophysical Research: Planets*, *127*(3), e2021JE007025. https://doi.org/10.1029/2021JE007025

Bire, S., Mittal, T., Kang, W., Ramadhan, A., Tuckman, P. J., German, C. R., et al. (2023). Divergent behavior of hydrothermal plumes in fresh versus salty icy ocean worlds. *Journal of Geophysical Research: Planets*, *128*(11), e2023JE007740. https://doi.org/10.1029/2023JE007740

Briggs, G. A. (1965). A plume rise model compared with observations. *Journal of the Air Pollution Control Association*, *15*(9), 433–438. https://doi.org/10.1080/00022470.1965.10468404

Briggs, G. A. (1982). Plume rise predictions. In *Lectures on air pollution and environmental impact analyses* (pp. 59–111). American Meteorological Society. https://doi.org/10.1007/978-1-935704-23-2_3

Busse, F. H. (1970). Thermal instabilities in rapidly rotating systems. *Journal of Fluid Mechanics*, *44*(3), 441–460. https://doi.org/10.1017/S0022112070001921

Čadek, O., Tobie, G., Van Hoolst, T., Massé, M., Choblet, G., Lefèvre, A., et al. (2016). Enceladus's internal ocean and ice shell constrained from Cassini gravity, shape, and libration data. *Geophysical Research Letters*, *43*(11), 5653–5660. https://doi.org/10.1002/2016GL068634

Choblet, G., Tobie, G., Sotin, C., Běhounková, M., Čadek, O., Postberg, F., & Souček, O. (2017). Powering prolonged hydrothermal activity inside Enceladus. *Nature Astronomy*, *1*(12), 841–847. https://doi.org/10.1038/s41550-017-0289-8

Collins, G. C., Head III, J. W., Pappalardo, R. T., & Spaun, N. A. (2000). Evaluation of models for the formation of chaotic terrain on Europa. *Journal of Geophysical Research*, *105*(E1), 1709–1716. https://doi.org/10.1029/1999JE001143

Crawford, T. V., & Leonard, A. S. (1962). Observations of buoyant plumes in calm stably stratified air. *Journal of Applied Meteorology and Climatology*, *1*(2), 251–256. https://doi.org/10.1175/1520-0450(1962)001⟨0251:OOBPIC⟩2.0.CO;2

Deremble, B. (2016). Convective plumes in rotating systems. *Journal of Fluid Mechanics*, *799*, 27–55. https://doi.org/10.1017/jfm.2016.348

Devenish, B. J., Rooney, G. G., & Thomson, D. J. (2010). Large-eddy simulation of a buoyant plume in uniform and stably stratified environments. *Journal of Fluid Mechanics*, *652*, 75–103. https://doi.org/10.1017/S0022112010000017

Fabregat Tomàs, A., Poje, A. C., Özgökmen, T. M., & Dewar, W. K. (2016). Effects of rotation on turbulent buoyant plumes in stratified environments. *Journal of Geophysical Research: Oceans*, *121*(8), 5397–5417. https://doi.org/10.1002/2016JC011737

Fernando, H. J. S., Chen, R.-r., & Ayotte, B. A. (1998). Development of A point plume in the presence of background rotation. *Physics of Fluids*, *10*(9), 2369–2383. https://doi.org/10.1063/1.869754

Frank, D., Landel, J. R., Dalziel, S. B., & Linden, P. F. (2017). Anticyclonic precession of a plume in a rotating environment. *Geophysical Research Letters*, *44*(18), 9400–9407. https://doi.org/10.1002/2017GL074191

Gastine, T., Wicht, J., & Aubert, J. (2016). Scaling regimes in spherical shell rotating convection. *Journal of Fluid Mechanics*, *808*, 690–732. https://doi.org/10.1017/jfm.2016.659

Goodman, J. C., Collins, G. C., Marshall, J., & Pierrehumbert, R. T. (2004). Hydrothermal plume dynamics on Europa: Implications for chaos formation. *Journal of Geophysical Research*, *109*(E3). https://doi.org/10.1029/2003JE002073

Goodman, J. C., & Lenferink, E. (2012). Numerical simulations of marine hydrothermal plumes for Europa and other icy worlds. *Icarus*, *221*(2), 970–983. https://doi.org/10.1016/j.icarus.2012.08.027

Greeley, R., Figueredo, P. H., Williams, D. A., Chuang, F. C., Klemaszewski, J. E., Kadel, S. D., et al. (2000). Geologic mapping of Europa. *Journal of Geophysical Research*, *105*(E9), 22559–22578. https://doi.org/10.1029/1999JE001173

Greenberg, R., Hoppa, G. V., Tufts, B., Geissler, P., Riley, J., & Kadel, S. (1999). Chaos on Europa. *Icarus*, *141*(2), 263–286. https://doi.org/10.1006/icar.1999.6187

Hansen, C. J., Esposito, L., Stewart, A. I. F., Colwell, J., Hendrix, A., Pryor, W., et al. (2006). Enceladus' water vapor plume. *Science*, *311*(5766), 1422–1425. https://doi.org/10.1126/science.1121254

Helfrich, K. R., & Battisti, T. M. (1991). Experiments on baroclinic vortex shedding from hydrothermal plumes. *Journal of Geophysical Research*, *96*(C7), 12511–12518. https://doi.org/10.1029/90JC02643

Hemingway, D. J., & Mittal, T. (2019). Enceladus's ice shell structure as a window on internal heat production. *Icarus*, *332*, 111–131. https://doi.org/10.1016/j.icarus.2019.03.011

Hoolst, T. V., Baland, R.-M., & Trinh, A. (2016). The diurnal libration and interior structure of Enceladus. *Icarus*, *277*, 311–318. https://doi.org/10.1016/j.icarus.2016.05.025

Hsu, H.-W., Postberg, F., Sekine, Y., Shibuya, T., Kempf, S., Horányi, M., et al. (2015). Ongoing hydrothermal activities within Enceladus. *Nature*, *519*(7542), 207–210. https://doi.org/10.1038/nature14262

Hunt, G. R., & Kaye, N. G. (2001). Virtual origin correction for lazy turbulent plumes. *Journal of Fluid Mechanics*, *435*, 377–396. https://doi.org/10.1017/S0022112001003871

Iess, L., Stevenson, D. J., Parisi, M., Hemingway, D., Jacobson, R. A., Lunine, J. I., et al. (2014). The gravity field and interior structure of Enceladus. *Science*, *344*(6179), 78–80. https://doi.org/10.1126/science.1250551

Kang, W. (2022). Different ice-shell geometries on Europa and Enceladus due to their different sizes: Impacts of ocean heat transport. *The Astrophysical Journal*, *934*(2), 116. https://doi.org/10.3847/1538-4357/ac779c

Kang, W., Bire, S., & Marshall, J. (2022). The role of ocean circulation in driving hemispheric symmetry breaking of the ice shell of Enceladus. *Earth and Planetary Science Letters*, *599*, 117845. https://doi.org/10.1016/j.epsl.2022.117845

Kang, W., Marshall, J., Mittal, T., & Bire, S. (2022). Ocean dynamics and tracer transport over the south pole geysers of Enceladus. *Monthly Notices of the Royal Astronomical Society*, *517*(3), 3485–3494. https://doi.org/10.1093/mnras/stac2882

Kang, W., Mittal, T., Bire, S., Campin, J.-M., & Marshall, J. (2022). How does salinity shape ocean circulation and ice geometry on Enceladus and other icy satellites? *Science Advances*, *8*(29), eabm4665. https://doi.org/10.1126/sciadv.abm4665

Kivelson, M. G., Khurana, K. K., Russell, C. T., Volwerk, M., Walker, R. J., & Zimmer, C. (2000). Galileo magnetometer measurements: A stronger case for a subsurface ocean at Europa. *Science*, *289*(5483), 1340–1343. https://doi.org/10.1126/science.289.5483.1340

Lefevre, A., Tobie, G., Choblet, G., & Čadek, O. (2014). Structure and dynamics of titan's outer icy shell constrained from Cassini data. *Icarus*, *237*, 16–28. https://doi.org/10.1016/j.icarus.2014.04.006

Legg, S., Jones, H., & Visbeck, M. (1996). A heton perspective of baroclinic eddy transfer in localized open ocean convection. *Journal of Physical Oceanography*, *26*(10), 2251–2266. https://doi.org/10.1175/1520-0485(1996)026⟨2251:AHPOBE⟩2.0.CO;2

List, E. J. (1982). Turbulent jets and plumes. *Annual Review of Fluid Mechanics*, *14*(1), 189–212. https://doi.org/10.1146/annurev.fl.14.010182.001201

Lobo, A. H., Thompson, A. F., Vance, S. D., & Tharimena, S. (2021). A pole-to-equator ocean overturning circulation on Enceladus. *Nature Geoscience*, *14*(4), 185–189. https://doi.org/10.1038/s41561-021-00706-3

Lucchitta, B., & Soderblom, L. (1982). The geology of Europa. In D. Morrison & M. D. Matthews (Eds.), *Satellites of Jupiter* (pp. 521–555). University of Arizona Press.

MacKenzie, S. M., Birch, S. P. D., Hörst, S., Sotin, C., Barth, E., Lora, J. M., et al. (2021). Titan: Earth-like on the outside, ocean world on the inside. *The Planetary Science Journal*, *2*(3), 112. https://doi.org/10.3847/PSJ/abf7c9

McDougall, T. (1981). Negatively buoyant vertical jets. *Tellus*, *33*(3), 313–320. https://doi.org/10.3402/tellusa.v33i3.10718

Morton, B. R. (1959). Forced plumes. *Journal of Fluid Mechanics*, *5*(1), 151–163. https://doi.org/10.1017/S002211205900012X

Morton, B. R., Taylor, G. I., & Turner, J. S. (1956). Turbulent gravitational convection from maintained and instantaneous sources. *Proceedings of the Royal Society of London. Series A. Mathematical and Physical Sciences*, *234*(1196), 1–23. https://doi.org/10.1098/rspa.1956.0011

Nimmo, F., Thomas, P., Pappalardo, R., & Moore, W. (2007). The global shape of Europa: Constraints on lateral shell thickness variations. *Icarus*, *191*(1), 183–192. https://doi.org/10.1016/j.icarus.2007.04.021

Pedlosky, J. (1987). *Geophysical fluid dynamics*. Springer.

Porco, C. C., Helfenstein, P., Thomas, P., Ingersoll, A., Wisdom, J., West, R., et al. (2006). Cassini observes the active south pole of Enceladus. *Science*, *311*(5766), 1393–1401. https://doi.org/10.1126/science.1123013

Postberg, F., Kempf, S., Schmidt, J., Brilliantov, N., Beinsen, A., Abel, B., et al. (2009). Sodium salts in e-ring ice grains from an ocean below the surface of Enceladus. *Nature*, *459*(7250), 1098–1101. https://doi.org/10.1038/nature08046

Postberg, F., Khawaja, N., Abel, B., Choblet, G., Glein, C. R., Gudipati, M. S., et al. (2018). Macromolecular organic compounds from the depths of Enceladus. *Nature*, *558*(7711), 564–568. https://doi.org/10.1038/s41586-018-0246-4

Powell, C. W., Haynes, P. H., Ming, A. D., & Taylor, J. R. (2025). Moisture transport by convective overshoots in the tropical tropopause layer. *Weather*, *80*(6), 206–213. https://doi.org/10.1002/wea.7689

Powell, C. W., Haynes, P. H., & Taylor, J. R. (2024). Diagnosing tracer transport in convective penetration of a stably stratified layer. *Journal of Fluid Mechanics*, *997*, A48. https://doi.org/10.1017/jfm.2024.662

Powell, C. W., Sutherland, B. R., Haynes, P. H., & Taylor, J. R. (2025). Internal waves generated by a plume impinging on a stratified fluid. *Journal of Fluid Mechanics*, *1006*, R2. https://doi.org/10.1017/jfm.2025.40

Ramadhan, A., Wagner, G. L., Hill, C., Campin, J.-M., Churavy, V., Besard, T., et al. (2020). Oceananigans.jl: Fast and friendly geophysical fluid dynamics on GPUs. *Journal of Open Source Software*, *5*(53), 2018. https://doi.org/10.21105/joss.02018

Rouse, H., shun Yih, C., & Humphreys, H. W. (1952). Gravitational convection from a boundary source. *Tellus A: Dynamic Meteorology and Oceanography*, *4*(3), 201–210. https://doi.org/10.3402/tellusa.v4i3.8688

Scase, M. M., Caulfield, C. P., & Dalziel, S. B. (2006). Boussinesq plumes and jets with decreasing source strengths in stratified environments. *Journal of Fluid Mechanics*, *563*, 463–472. https://doi.org/10.1017/S0022112006000784

Shu, C.-W. (2009). High order weighted essentially nonoscillatory schemes for convection dominated problems. *SIAM Review*, *51*(1), 82–126. https://doi.org/10.1137/070679065

Silvestri, S., Wagner, G. L., Campin, J.-M., Constantinou, N. C., Hill, C. N., Souza, A., & Ferrari, R. (2024). A new weno-based momentum advection scheme for simulations of ocean mesoscale turbulence. *Journal of Advances in Modeling Earth Systems*, *16*(7), e2023MS004130. https://doi.org/10.1029/2023MS004130

Soderlund, K. M. (2019). Ocean dynamics of outer solar system satellites. *Geophysical Research Letters*, *46*(15), 8700–8710. https://doi.org/10.1029/2018GL081880

Soderlund, K. M., Kalousová, K., Buffo, J. J., Glein, C. R., Goodman, J. C., Mitri, G., et al. (2020). Ice-ocean exchange processes in the Jovian and saturnian satellites. *Space Science Reviews*, *216*(5), 80. https://doi.org/10.1007/s11214-020-00706-6

Speer, K. G., & Marshall, J. (1995). The growth of convective plumes at seafloor hot springs. *Journal of Marine Research*, *53*(6), 1025–1057. https://doi.org/10.1357/0022240953212972

Spohn, T., & Schubert, G. (2003). Oceans in the icy Galilean satellites of Jupiter? *Icarus*, *161*(2), 456–467. https://doi.org/10.1016/S0019-1035(02)00048-9

Sutherland, B., Ma, Y., Flynn, M., Frank, D., Linden, P., Lemasquerier, D., et al. (2021). Plumes in rotating fluid and their transformation into tornados. *Journal of Fluid Mechanics*, *924*, A15. https://doi.org/10.1017/jfm.2021.618

Tarshish, N., & Romps, D. M. (2022). A closure for the virtual origin of turbulent plumes. *Journal of the Atmospheric Sciences*, *79*(5), 1459–1471. https://doi.org/10.1175/JAS-D-21-0096.1

Thomas, P., Tajeddine, R., Tiscareno, M., Burns, J., Joseph, J., Loredo, T., et al. (2016). Enceladus's measured physical libration requires a global subsurface ocean. *Icarus*, *264*, 37–47. https://doi.org/10.1016/j.icarus.2015.08.037

Thomson, R. E., & Delaney, J. R. (2001). Evidence for a weakly stratified European ocean sustained by seafloor heat flux. *Journal of Geophysical Research*, *106*(E6), 12355–12365. https://doi.org/10.1029/2000JE001332

Turner, J. S. (1973). *Buoyancy effects in fluids*. Cambridge University Press.

Turner, J. S. (1986). Turbulent entrainment: The development of the entrainment assumption, and its application to geophysical flows. *Journal of Fluid Mechanics*, *173*, 431–471. https://doi.org/10.1017/S0022112086001222

Vance, S., Goodman, J., & Dotson, R. (2009). Oceanography of an ice-covered moon. In *Europa* (pp. 459–482). University of Arizona Press. Retrieved from http://www.jstor.org/stable/j.ctt1xp3wdw.25

Vance, S., Harnmeijer, J., Kimura, J., Hussmann, H., deMartin, B., & Brown, J. M. (2007). Hydrothermal systems in small ocean planets. *Astrobiology*, *7*(6), 987–1005. https://doi.org/10.1089/ast.2007.0075

Vance, S. D., Panning, M. P., Stähler, S., Cammarano, F., Bills, B. G., Tobie, G., et al. (2018). Geophysical investigations of habitability in ice-covered ocean worlds. *Journal of Geophysical Research: Planets*, *123*(1), 180–205. https://doi.org/10.1002/2017JE005341

Visbeck, M., Marshall, J., & Jones, H. (1996). Dynamics of isolated convective regions in the ocean. *Journal of Physical Oceanography*, *26*(9), 1721–1734. https://doi.org/10.1175/1520-0485(1996)026⟨1721:doiCRI⟩2.0.CO;2

Waite, J. H., Combi, M. R., Ip, W.-H., Cravens, T. E., McNutt, R. L., Kasprzak, W., et al. (2006). Cassini ion and neutral mass spectrometer: Enceladus plume composition and structure. *Science*, *311*(5766), 1419–1422. https://doi.org/10.1126/science.1121290

Waite, J. H., Glein, C. R., Perryman, R. S., Teolis, B. D., Magee, B. A., Miller, G., et al. (2017). Cassini finds molecular hydrogen in the Enceladus plume: Evidence for hydrothermal processes. *Science*, *356*(6334), 155–159. https://doi.org/10.1126/science.aai8703

Wang, S. (2025). Data for rotating penetrative plume [Dataset]. *Zenodo*. https://doi.org/10.5281/zenodo.18109486

Wang, S., Kang, W., Zhang, Y., & Marshall, J. (2025). The fate of rotating point plumes in an unstratified environment: From free growth to boundary interactions. *Journal of Fluid Mechanics*, *1018*, A19. https://doi.org/10.1017/jfm.2025.10533

Whitehead, J. A., Marshall, J., & Hufford, G. E. (1996). Localized convection in rotating stratified fluid. *Journal of Geophysical Research*, *101*(C11), 25705–25721. https://doi.org/10.1029/96JC02322

Zeng, Y., & Jansen, M. F. (2021). Ocean circulation on Enceladus with a high-versus low-salinity ocean. *The Planetary Science Journal*, *2*(4), 151. https://doi.org/10.3847/PSJ/ac1114

Zhang, W., He, Z., & Jiang, H. (2017). Scaling for turbulent viscosity of buoyant plumes in stratified fluids: Piv measurement with implications for submarine hydrothermal plume turbulence. *Deep Sea Research Part I: Oceanographic Research Papers*, *129*, 89–98. https://doi.org/10.1016/j.dsr.2017.10.006

Zhang, Y., Bire, S., Wang, S., Nath, A., Ramadhan, A., Kang, W., & Marshall, J. (2025). Long transit time from the seafloor to the ice shell on enceladus. *Monthly Notices of the Royal Astronomical Society*, *541*(2), 859–871. https://doi.org/10.1093/mnras/staf1008

Zhang, Y., Kang, W., & Marshall, J. (2024). Ocean weather systems on icy moons, with application to Enceladus. *Science Advances*, *10*(45), eadn6857. https://doi.org/10.1126/sciadv.adn6857

Zhu, P., Manucharyan, G. E., Thompson, A. F., Goodman, J. C., & Vance, S. D. (2017). The influence of meridional ice transport on Europa's ocean stratification and heat content. *Geophysical Research Letters*, *44*(12), 5969–5977. https://doi.org/10.1002/2017gl072996

Zimmer, C., Khurana, K. K., & Kivelson, M. G. (2000). Subsurface oceans on Europa and Callisto: Constraints from Galileo magnetometer observations. *Icarus*, *147*(2), 329–347. https://doi.org/10.1006/icar.2000.6456